DMB

DATABASE MANAGEMENT AND BIOMETRICS

.47057

UNDERSTANDING AND MODELLING THE VASCULAR BIOMETRIC IMAGING PROCEDURE

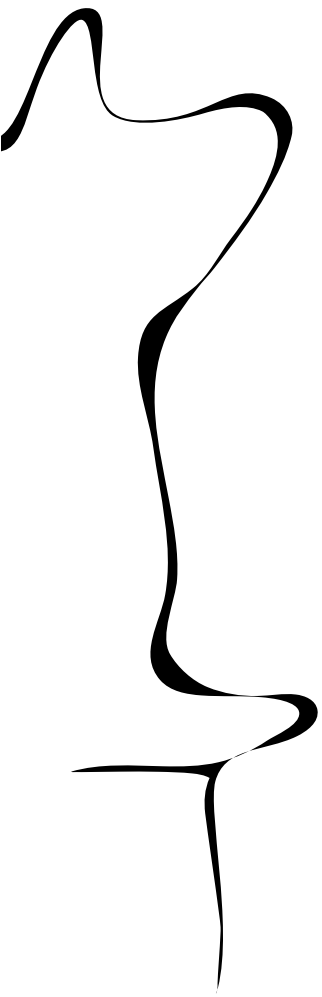## Muriel van der Spek

MASTERS THESIS ASSIGNMENT

Committee:
Luuk Spreeuwers
Tugce Arican
Loes Segerink
Kenan Niu

July, 2022

UNIVERSITY OF TWENTE. | **DIGITAL SOCIETY INSTITUTE**

Understanding and Modelling the Vascular Biometric Imaging Procedure

Muriel van der Spek

Faculty of Electrical Engineering, Mathematics and Computer Science (EEMCS),
Data Management & Biometrics (DMB), University of Twente, 7500 AE Enschede, The Netherlands

Abstract—In finger vascular biometric images, captured with near-infrared (NIR) light, several structures are visible, from which the exact origin is unknown. These include the vagueness, width and intensity of the vessel projection, the brightness of the two joints and the intensity of the dark area between the joints. These features vary per subject. To understand the origin of these elements, the imaging procedure is mimicked using a simplified mathematical model of the finger. This model creates images similar to real finger vascular images incorporating basic anatomy and corresponding optical properties. Using the model, the origin of several features is examined. The vessels appear vague, because the projection is actually a shadow caused by the strong scattering of the bone. The intensity of the finger (besides the vessels) is directly dependent on both tissue consistency (amount of absorption/scattering) and finger anatomy (path length of the photons). This research gives an insight on the vascular imaging procedure and this knowledge can be used in future research on vascular biometric identification, by incorporating additional features from the images.

Index Terms—Beer-Lambert, Effective Attenuation Coefficient, Finger Vein Images, Maximum Curvature, Vascular Biometrics, UTFVP Dataset

I. Introduction

Vascular biometric identification systems have widely proven to be very effective in terms of privacy, robustness and identification performance, since this biometric feature is hidden from the naked eye and changes minimally over the years [1]. Current vascular identification systems are mainly focused on the vascular pattern in the sclera, hand palm and the finger. Vessels in the finger can be captured with near-infrared (NIR) light, where they appear as dark shadow-like patterns, see figure 1. These images are captured with 850 nm, which is a wavelength that the haemoglobin strongly absorbs.

In the two images in figure 1, the visibility of each vessel is very different, referring to its vagueness, width and intensity. The joints light up in NIR images, and both the intensity of the joints and contrast of the borders is different in the two images. The intensity
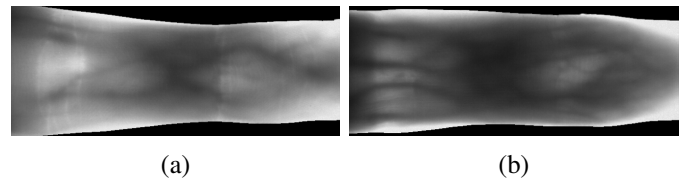

Fig. 1: Example NIR images of the finger from the UTFVP dataset made with the finger vessel scanner at the University of Twente [2]. The fingers point to the right.

of the dark area between the joints is also varying. These variations are not uncommon, they are different per subject. Interestingly, there is not much known about the origin of these variations.

This thesis will focus on understanding the origin of aforementioned features in the finger vascular images, in order to better understand the imaging process. For this reason, the influence of finger anatomy and optical properties of the tissues needs to be examined. This is done by creating a system that generates vascular images including both anatomical and optical information.

The main objective of this research is to provide an explanation for why the finger vascular NIR images appear as they do. Several research questions are relevant, in order to get an understanding of the vessel pattern inside the finger, and the way that it is captured.

1) Which biological tissues in the finger are crucial in the imaging procedure?
2) Why are the vessels vague?
3) Why is the area between the joints in some images much darker than in other images?
4) How can transmission of NIR light through the finger be modelled?
5) Can the original vessel templates be recovered from generated images?

Obtaining knowledge on the origin of all features in the NIR images can make the identification process even more robust and accurate, and can also be used in research on spoofing.

The remainder of this paper is as follows. First, a brief background is presented on both the anatomical terminology and relevant optical properties in section II and III. The function of these sections is to give a basic understanding of the finger anatomy on which the model is based, and the optical formulas that form the mathematical base. The related work is discussed in section IV, followed by the method in section V. An introduction to the experiments is discussed in section VI, followed by the corresponding results in section VII. The discussion in section VIII uses the obtained results to answer the aforementioned research questions. A final conclusion is provided in section IX.

II. ANATOMICAL BACKGROUND

Due to the nature of finger vascular biometrics, a large part of this research concerns the anatomy of the finger. This section gives an overview of the anatomy of the finger and the relevant terminology.

A. Skin

The human skin consists of three layers: the epidermis, dermis and subcutis. The epidermis is the most outer layer, the dermis is the middle layer, and the subcutis is the layer surrounding the bone containing fat cells. Together, the epidermis and dermis have an approximately constant thickness of less than 1 mm [3], [4]. The vessels visible in NIR illumination mainly lie in the subcutis skin tissue. The thickness of the subcutis layer is directly depending on the amount of body fat. Additional variations for the thickness of each skin layer may include temperature, humidity, solar exposure, gender, age and race, as discussed in chapter 4 and 5 of [5].

B. Bones

Each hand contains 14 bones, named phalanges, three per finger except for the thumb, which has only 2. A schematic image is shown in figure 2. From the fingertip to the hand palm, the phalanges are respectively called the distal phalanx (DP), middle phalanx (MP) and proximal phalanx (PP). The two joints that are visible in the NIR images for vascular biometrics are the proximal interphalangeal (PIP) joint and the distal interphalangeal (DIP) joint. Each phalanx has a head, shaft and base. The shaft is much thinner and has an oval shape compared to the round head and base. For vascular biometrics, normally only the index, middle and ring finger are used, since the thumb has a different bone structure, and the little finger is too short.
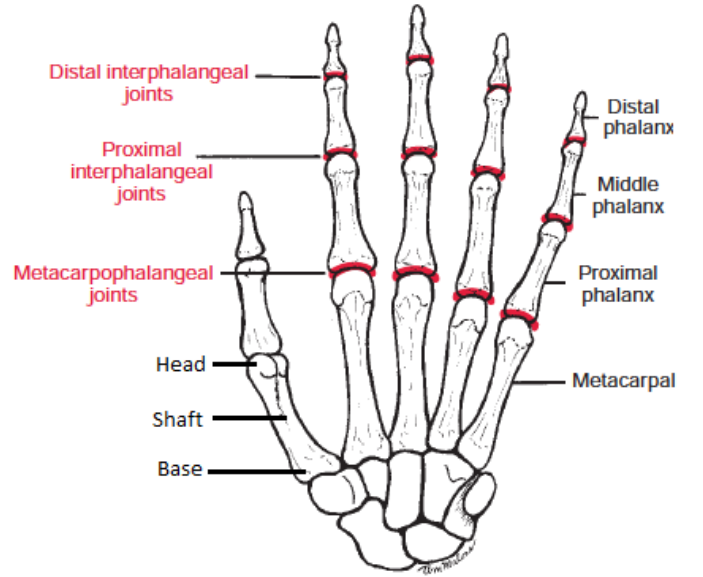

Fig. 2: Bones in a human hand [6].

C. Finger vessels

Arteries are oxygen-rich, meaning that they supply blood to the organs. They contain oxygenated haemoglobin (HbO_2). Veins are oxygen-low, bringing the deoxygenated blood (Hb) back to the heart. Each finger contains two proper palmar digital arteries, one on each side of the finger, from the hand palm to the fingertip. The branching of these vessels contribute to the unique pattern visible in NIR images. The images shown in figure 3 show three example visibility stages of the proper palmar digital arteries.

(a) Visible.

(b) Ambiguous.
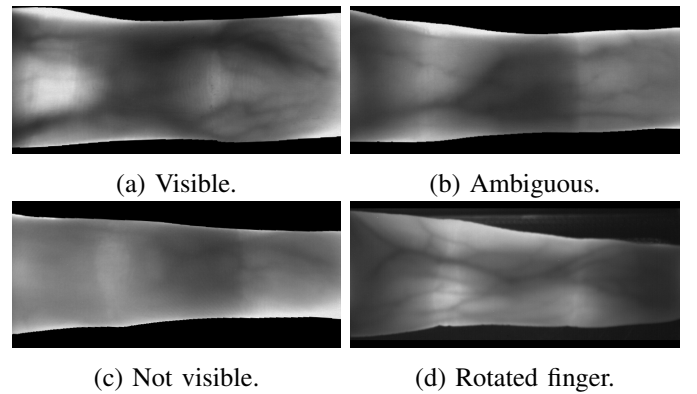
(c) Not visible.

(d) Rotated finger.

Fig. 3: Visualisation of the different visibility stages of the two proper digital arteries in the UTFVP dataset [2] in (a, b, c). Additionally, a rotated finger is added in (d) to visualise the artery from the side.

III. OPTICAL BACKGROUND

This section is meant to give a brief background on optical phenomena, that may change either the direction

or intensity of a photon, with the focus on biological tissues. Additionally, the equations to describe these phenomena are introduced.

The Beer-Lambert law, see equation 1, can be used to express the amount of absorption and scattering in a medium. Here, I_0 is the intensity of the incoming light, I is the intensity of the light leaving the medium in the same direction as I_0, d is the thickness of the medium and the term μ represents the amount of absorption and scattering.

$$I = I_0 e^{-\mu d} \tag{1}$$

Absorption is the phenomenon where a photon collides with a particle inside the medium and loses its energy. The absorption coefficient μ_a defines the amount of absorption of photons in a medium at a wavelength, expressed in mm^{-1}. Using the Beer-Lambert law from equation 1, the output intensity can be calculated by substituting $\mu = \mu_a$, assuming the medium does not scatter.

Scattering is the phenomenon where a particle collides with a particle inside the medium and changes direction, defined by μ_s (equivalent to μ_a). The direction of scattering light in biological tissue is often diffuse, meaning that scattering in any direction is theoretically possible. However, the average scattering angle $\bar{\theta}$ in biological tissues is often not zero. Therefore, the reduced scattering coefficient μ'_s is normally used to represent the scattering. In short, this is a modified version of μ_s that includes the average scattering angle, see formula 2. The reduced scattering coefficient uses the anisotropy factor g of the tissue, which is the cosine of the average scattering angle, thus $g = \cos(\bar{\theta})$.

$$\mu'_s = \mu_s(1 - g) \tag{2}$$

In an anisotropic diffuse medium such as biological tissues, both absorption and scattering occur. Scattering increases the total path length of the photons, giving it a higher chance to be absorbed. These coefficients are combined in the effective attenuation coefficient μ_{eff}, see equation 3, which can be used in the Beer-Lambert law in equation 1.

$$\mu = \mu_{eff} = \sqrt{3\mu_a(\mu_a + \mu'_s)} \tag{3}$$

IV. RELATED WORK

This section gives an overview of literature related to obtaining an understanding on the visual effect of biological tissues in NIR images.

A. Generating synthetic finger vascular images

The research in [7] presents a method to create synthetic finger vessel images. They first generate the vessel tree structure, then include two bright joints, and finish with image processing techniques, to resemble real finger vascular images. An example synthetic image is shown in figure 4a.

(a) Result from [7].   (b) Result from [8].

Fig. 4: Synthetic vascular finger images from literature.

A few years after this publication, [8] uses a Generative Adversarial Network (GAN) to generate synthetic vessel images. A resulting synthetic image is shown in 4b. In short, a GAN is a neural network architecture containing a generator and a discriminator network. The generator learns to generate the synthetic images, and the discriminator learns to classify real and synthetic images. Further understanding GANs is outside the scope of this research, but the interested reader can find more information in the introduction of [9] and [10].

The two studies previously discussed are solely based on generating an image that resembles a real image, but the research presented in [11] goes in a different direction. They used a simplified mathematical model of the finger, where the projection is calculated based on an approximation of the light transmission trough a real finger. Here, the absorption coefficient μ_a of subcutis is used to obtain an expression for the transmission, neglecting the scattering.

B. Vessel extraction methods

Chapter 1.3.1 of [1] gives an extensive overview of vessel extraction methods for vascular biometrics. A visualisation of the resulting templates from tree common extraction methods is given in figure 5 [12]. Note that the image in figure 5b looks most similar to the vessel structure in the original image. An overview of algorithms with their original paper is presented in table VII of appendix B.

The performance of a feature extraction method is often expressed in terms of the equal error rate (EER), which is the identification error, explained in section V-C. The performance may be influenced by the dataset capturing procedure and pre-processing steps [2]. When algorithms are compared on the same dataset, with the same pre-processing steps, the most unbiased
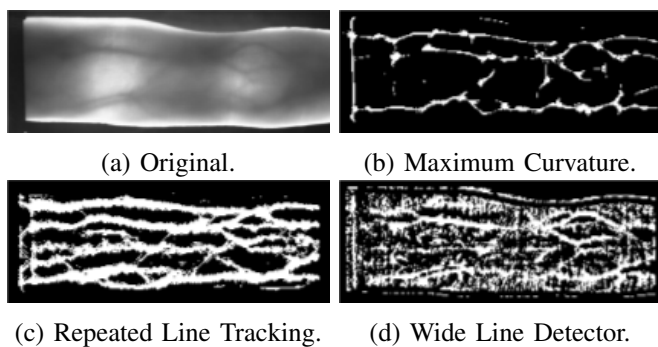
(a) Original.

(b) Maximum Curvature.

(c) Repeated Line Tracking.

(d) Wide Line Detector.

Fig. 5: Visualisation of three extraction methods [12].

TABLE I: Overview of the mean μ_a, μ_s' and resulting μ_{eff} with standard deviation in mm^{-1}.

Tissue	μ_a	μ_s'	μ_{eff}
Subcutis	0.094	1.21	0.61 ± 0.16
Bone	0.023	1.56	0.33 ± 0.18
Blood	0.48	1.70	1.77 ± 0.27

conclusion can be drawn on the resulting performance. For this reason, the most optimal algorithm is not chosen based on the original paper, but rather on studies that compare multiple algorithms. Table VIII in appendix B contains an overview of the EER scores from comparing studies. Maximum Curvature (MC) gives the lowest EER in 4 out of 7 studies.

The steps to obtain a binary vessel template using MC are accurately described in the original paper [13]. Additionally, Bram Ton made a Matlab implementation of this algorithm available [14], which he applied in [2].

C. Optical coefficients

Relevant optical variables are the reduced scattering coefficient μ_s' and absorption coefficient μ_a. If only μ_s is known, the anisotropy factor g is needed as well to calculate μ_s'. With these coefficients, the effective attenuation coefficient μ_{eff} of the respective tissue can be obtained.

Values for μ_s', μ_a and the resulting μ_{eff} are summarised in table I. Tables III, IV and V in appendix A give an overview of the literature used to calculate these average values. Table VI in the same appendix gives anisotropy factors for various tissue types, where 0.9 is a very common value to use. Due to lack of optical data on human samples, or lack of precise anatomical information related to the finger, the dermis, epidermis and articular cartilage are not included in the optical overview.

To calculate the absorption coefficient of blood, the molar extinction coefficients presented in the respective studies are used with a molar concentration of 2.303 and the haemoglobin gram molecular weight of 66,500. Both the absorption and scattering of HBO$_2$ are slightly higher than for Hb. The values for blood in table I represent the average, since in finger vascular images, there is no clear distinction between veins and arteries.

Several factors directly influence the amount of absorption and scattering in subcutis, bone and blood

samples. First, for the bone, the amount of demineralization [15] and the location of the sample [16] influence the amount of scattering. Thus, the scattering depends on whether the bone sample contains for example inner sponge structure or the solid bone surface structure. For the subcutis, the sample location also influences the scattering, due to the different amounts of connective tissue [17]. Additionally, the increasing ratio of water over fat cells appears to increase the absorption [18]. For blood, increasing the haemoglobin concentration increases both absorption and scattering [19].

D. Conclusion

The mentioned studies on generating synthetic finger vascular images do not include anatomical and optical information. Since it is desired to obtain an understanding for the imaging process of finger vascular images, the simplified mathematical model from [11] will be used as a starting point. The optical coefficients for subcutis, bone and the vessels from table I will be used in the model. The vessel template will be extracted using MC, since this method proves to be the most effective. The Matlab implementation [14] will function as a starting point.

V. METHOD

A. Data pre-processing and vessel extraction

The UTFVP dataset is used to provide the vessel patterns. Two example images from this set are shown in figure 1 in the introduction. This set is chosen due to the fact that these images are made with the sensor at the University of Twente, and their capturing is very well documented [2]. Pre-processing the images includes detecting the finger region, aligning the finger horizontally, removing the background and increasing the visibility of the vessels using histogram equalisation [1]. This results in figure 6a.

A binary vessel template is extracted from the pre-processed images with MC, using the implementation presented in [14]. Additionally, the thickness of the binary vessels is enhanced to represent thickness of the vessels in the original image, see figure 6. This is done by applying a Gaussian filter over the whole image, and making all non-zero pixels white.
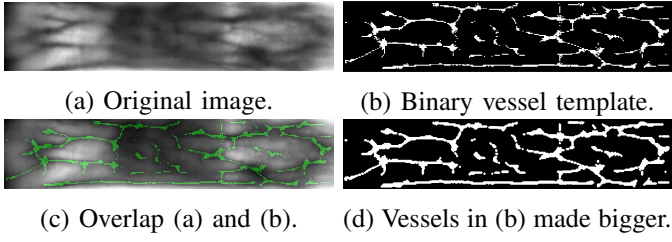
(a) Original image. (b) Binary vessel template.

(c) Overlap (a) and (b). (d) Vessels in (b) made bigger.

Fig. 6: Visualisation of the obtained vessel pattern.

B. Simplified mathematical model

The model represents a simplified human finger, consisting of bone, vessels and subcutis tissue, see the schematic in 7. Referring to research question 1, these three tissues are expected to be essential, since they take up the most space in the finger.

Eight light sources shine on the top of the bone, since the sensor at the University of Twente used to capture the UTFVP dataset also contains eight sources [2]. The finger is represented by a 6 cm long cylinder with a 17 mm diameter. Both the diameter and the centre of the bone are described by polynomials. The diameters of the PIP and DIP are respectively chosen to be 12 and 11 mm, and the shaft of the MP is 6 mm. The centre of the bone is lifted to make the top part of the bone at the same height over the whole finger. The depth of the vessels is defined linearly with the depth of the bone centre. The depth at the deepest point (shaft MP) is 1.5 mm deeper than at the most superficial point (PIP joint).
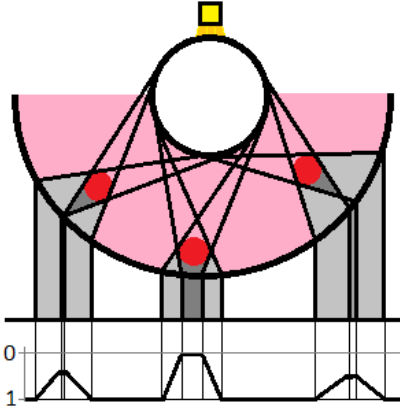

Fig. 7: Schematic model of the principle of the projection on the skin. Yellow square on top of the bone represents a light source. Red circles are the vessels and pink structure is the subcutis.

Referring to research question 4, the transmission can be modelled using the effective attenuation coefficients as presented in section IV-C and the Beer-Lambert equation discussed in section III. The transmission is obtained by tracing the photons in their journey from the light source through the bone, subcutis and optionally a vessel, until they reach the surface of the skin, see figure 7. The calculations inside the model will be divided into smaller parts to simplify the total projection. First, a dimensional reduction is done by dividing the model of the finger in thin slices, to obtain the vessel projection per slice, as visualised in the aforementioned figure. Combining the projections of the slices together forms the complete vessel projection on the surface of the skin. A parallel transformation is used to transform the cylindrical projection to the flat image plane.

The optical properties of the bone, subcutis and vessels, respectively μ_{eff_b}, μ_{eff_s} and μ_{eff_v}, define the output intensity I on the surface of the skin. First, the light enters the finger at the dorsal side of the bone (neglecting the skin above the bone), as shown in figure 7. The light travels to the bottom half of the bone with path length d_b. The photons then travel trough the subcutis tissue with length d_s. If a photon intersect with a vessel, the path trough the subcutis decreases with d_v. The transmission of one photon is expressed by equation 4, using the mean values as presented in table I.

$$\begin{aligned} I &= I_0 e^{-\mu_{eff_b} d_b - \mu_{eff_s}(d_s - d_v) - \mu_{eff_v} d_v} \\ &= I_0 e^{-0.33 d_b - 0.61(d_s - d_v) - 1.77 d_v} \end{aligned} \quad (4)$$

The model is constructed to calculate the transmission per slice, but in reality, the photons travel in every direction, thus the photons in the finger-length direction need to be included for both the bone and the subcutis. Scattering in the bone is incorporated by tracing the photons from each source to each location on the bottom surface of the bone in an arbitrary slice. The euclidean distance between the sources and the bone is used in the Beer-Lambert equation, and the intensity of the photons is attenuated accordingly. Equivalently, scattering in the subcutis can be obtained by tracing all photons from the bottom side of the bone to the surface of the finger of neighbouring slices. However, for the subcutis scattering, this drastically increases the amount of calculations. Therefore, an approximation of the scattering behaviour in this medium is done. One simplification is that in every slice of the finger, the distance from the bone to the skin (d_{old}) is the same. If the current slice is x, then the effects of the photons in the next slice $x + \Delta x$ can be calculated with the Beer-Lambert equation.

$$\frac{I}{I_0} = e^{-\mu_{eff} d_{new}} \quad (5)$$

With Pythagoras, the new distance d_{new} from the bone in slice x to the surface in slice $x + \Delta x$ is obtained.

$$d_{new} = \sqrt{\Delta x^2 + d_{old}^2}$$

The complete image can be shifted Δx and attenuated by a factor calculated with equation 5. Doing this for a wide range, and adding all the attenuated shifted images together, the scattering in the subcutis is approximated.

C. Model evaluation

The model is evaluated manually, based on whether the generated images visualise the expected behaviour. The aspects that are evaluated in this stage are furthermore discussed in the experiment section, and mainly cover the effect of varying the depth of vessels and optical coefficients of the subcutis and bone.

A mathematical expression for the similarity between two images can be obtained with normalised cross-correlation. Here, one image is shifted over a second image in both x- and y-direction, and the similarity, which is a value between -1 and 1, is calculated every instance (x, y). At some point, there is a maximum similarity, which represents the resulting similarity score. A distinction is made between genuine and impostor comparisons.

- **Genuine scores**: similarity between two images of the same source (same finger)
- **Impostor scores**: similarity between two images of different sources (two different fingers)

Naturally, genuine comparisons should have a large similarity score, and impostor comparisons a low score. The classification performance of an identification system is defined by the amount of overlap between the genuine and impostor distributions. The identification performance is defined by the false match rate (FMR) and false non-match rate (FNMR), see formula 6. These calculations use the amount of true positive (TP), true negative (TN), false positive (FP) and false negative (FN) classifications at a certain threshold.

$$FMR = \frac{FP}{FP + TN}$$
$$FNMR = 1 - \frac{TP}{TP + FN} \qquad (6)$$

The FMR and FNMR are calculated for the whole range of similarity scores. At some score, the FMR and FNMR are equal. This similarity score represents the decision threshold, which is the optimal similarity score to determine whether the inputs are a match. The equal error rate (EER) is the value of the FMR and FNMR at this decision threshold, which is a general measure that defines the performance of an identification system. The mathematical expression for the EER is given by equation 7.

$$EER = \arg\min |FMR - FNMR| \qquad (7)$$

VI. Experiments

There are four experiments, which are introduced in the next list.

1) **Evaluation of the possible vessel depths**. This experiment is meant to answer research question 2, to find whether there is a possible relation between the vagueness and depth. The exact depth inside the finger is unknown, but placing a template in the model at various depths, the projection can be compared with the vessels in the original image. Note that this depth differs per subject, thus this experiment only gives an indication for the used subject. For this experiment, the depth of the vessels at the PIP joint will vary between 0.25 and 1.25 mm, with steps of 0.25 mm. At the deepest point, which is around the shaft of the MP, the depth of the vessels will be increased an additional 1.5 mm.

2) **The effect of varying** μ_{eff}. Various values within the SD range for both bone and subtucis are tested. Both tissue structure and thickness (path length) is different per person, thus this experiment only gives an indication for the values representative for this model. This experiment is meant to answer research question 3, whether the different optical coefficients per subjects may be the source for the intensity differences at the MP.

3) **Evaluation of the chosen** μ_{eff}. When one light source is used to illuminate the finger, the resulting bright area gives information on the scattering angle. This effect can be mimicked in the model by using only one light source. Using these results, the chosen approach to approximate light transmission through the finger can be evaluated, referring to research question 4.

4) **Identification system based on generated images**. The genuine and impostor distributions from both real and generated images give insights on the basic similarity between the two, which can be compared on their mean value, standard deviation, decision threshold and EER as described in section V-C. This experiment is meant to answer research question 5. The cross-correlation score is a direct representation of how similar template from the generated image is to the original template from the real image.

VII. Results

Several features are added step-by-step in figure 8, visualising the effect of the biological tissues on the generated images.
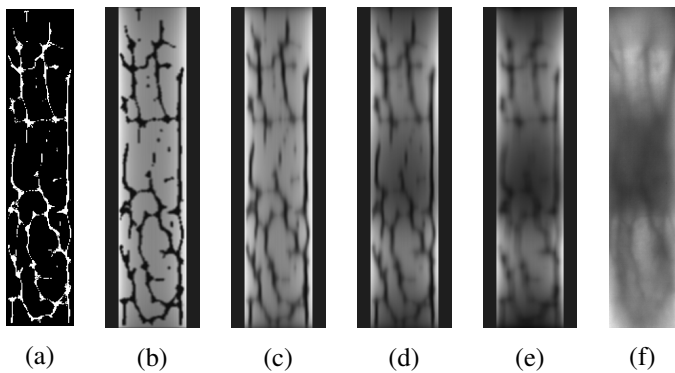
Fig. 8: Visualisation of the steps taken to obtain the final image. (a): Input template. (b): Bone with constant diameter, constant vessel depth. (c): Scattering of the subcutis. (d): Varying bone depth and diameter. (e): Vessel depth increases linearly with the centre of the bone. (f): Original image.

The results of experiment 1 are presented in figure 9, where the template is placed at varying depths in the model. Here the mentioned depth is the depth at the PIP joint, and increases an additional 1.5 mm at the shaft of the MP. Appendix C shows some additional images including the resulting template extracted with MC. The original image contains vessels at various sizes, where the generated images only contains vessels with a constant width. The vessels at the PIP joint and smaller vessels at the DIP joint appear to be most similar with a depth of 0.25 mm. The biggest vessel, at the right side of the image, has a width similar to the vessels in the image at a depth of 1.25 mm. Nevertheless, deep vessel appear to show strange behaviour, further elaborated in section VIII-B.
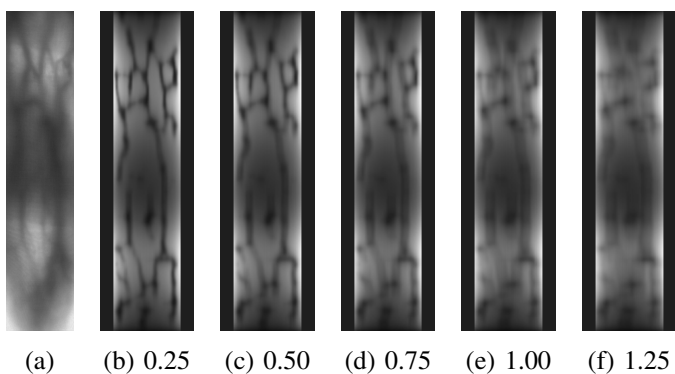

Fig. 9: Results of experiment 1. Varying vessel depths in mm. Original image in (a).

The resulting images for varying μ_{eff} of subcutis and bone are given in figures 10 and 11, corresponding to experiment 2. For both tissues, values close to the mean μ_{eff} appear to represent the original images best. Thus, for the subcutis 0.6 mm^{-1}, and for the bone 0.3 mm^{-1}. Values too far from these coefficients either result in overall too dark images, or are too bright at the MP compared to the joints. The image sets show opposite behaviour, where increasing μ_{eff} of the subcutis corresponds to decreasing μ_{eff} for the bone.
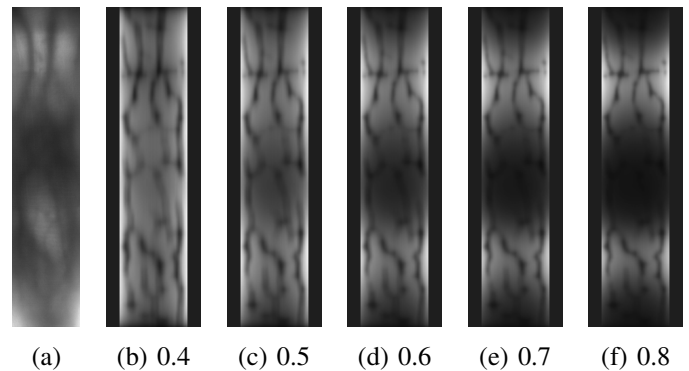

(a) (b) 0.4 (c) 0.5 (d) 0.6 (e) 0.7 (f) 0.8

Fig. 10: Resulting images of experiment 2. Here, μ_{eff} of subcutis is increased, expressed in mm^{-1}. Original image in (a).

(a) (b) 0.1 (c) 0.2 (d) 0.3 (e) 0.4 (f) 0.5
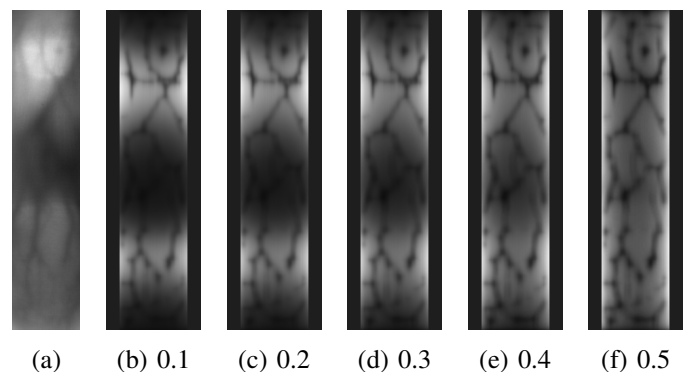
Fig. 11: Resulting images of experiment 2. Here, μ_{eff} in the bone is increased, expressed in mm^{-1}. Original image in (a).

The results of experiment 3 are shown in figure 12. The widths of the resulting areas are given in the image caption. The estimated length of the real finger in the image frame is 5 cm, where the finger in the model has a length of 6 cm. The width at the MP is approximately the same, and at the DIP, the generated area is slightly smaller.

Experiment 4 concerns the genuine and impostor distributions for real and generated images, shown in figure 13. An overview of the results obtained from the distributions is given in table II, based on the additional graphs in appendix D. The genuine distributions are very similar. The high error for the generated images is

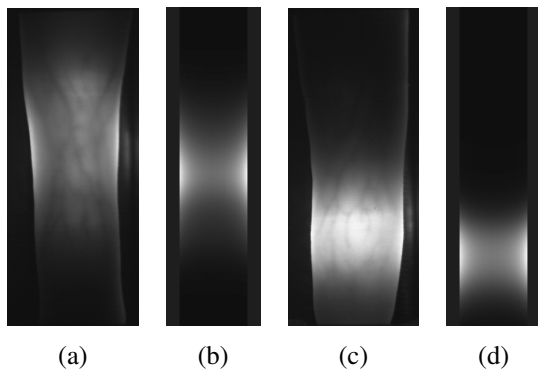Fig. 12: Results of experiment 3. Real (a, c) and generated (b, d) images visualising the effects of 1 light source above the MP (a, b) and DIP joint (c, d). Sizes of the illuminated areas from (a) to (d) are approximately 3.0 cm, 2.9 cm, 2.5 cm and 2.0 cm.

introduced by the average impostor scores being higher and the distribution is less steep compared to the real images.
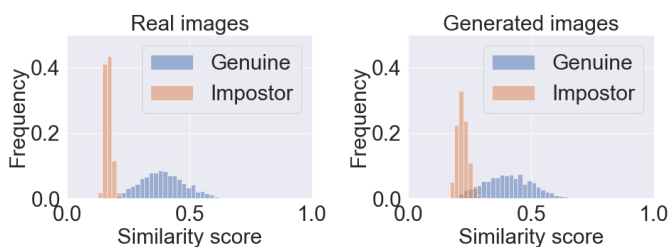

Fig. 13: Resulting distributions of experiment 4. Genuine and impostor similarity score distributions of the real and the generated images.

TABLE II: Results of experiment 4. Summary of the values obtained from the plots in figure 13.

	Genuine		Impostor		Decision	EER
Dataset	Mean	SD	Mean	SD	threshold	[%]
Real	0.392	0.090	0.167	0.014	0.210	0.74
Generated	0.406	0.097	0.220	0.023	0.256	6.60
Difference	0.014	0.007	0.053	0.009	0.046	5.86

VIII. DISCUSSION

In this study on vascular biometrics, the origin of several aspects in the images is examined. The following sections will use the results from the previous section to answer the research questions presented in the introduction. The last section presents a brief introduction on how to apply this work in future research.

A. Which tissues are crucial in the imaging procedure?

In the method, see section V, the assumption is made that the largest structures in the finger, thus the bones, subcutis and vessel pattern, are the main contributors to the imaging process. For a simplified model of the finger, this appears accurate since the generated images roughly represent the original images. Since the neglected tissues are much smaller, it is expected that they would only add details to the image. These additional tissues are the articular cartilage, tendons, ligaments that keep the tendons in place and synovial fluid between the joints. The joints are complex structures that are simplified in the model to the point that it is solid bone tissue with a large diameter. It is expected that especially including the tendons and the ligaments will improve the appearance of the generated images. The tendons take up a relatively large amount of space that is now assumed to be subcutis. The ligaments would be a good addition because it is expected that these bands around the joints are the cause for the rectangular joint shapes.

B. Why are the vessels vague?

A vague projection is only produced for vessels with a full-shadow (see the middle vessel in figure 7), which are at depths 0.25 and 0.5 in figure 9. From this, it can be concluded that there is a relation between the vessel depth and vagueness, and that in real images, vaguer vessels are likely deeper. Thus, to answer the research question, the vessels are vague because they are a shadow projection on the skin, where the bone acts as a light source.

Nevertheless, it is expected that the vessels would still show this behaviour when the depth is further increased. At stages where the vessels only produce half-shadows (see the right vessel in figure 7), the vessels appear to have a constant gray value with abrupt borders. This is something that is not visible in real images, and may be the result of the chosen μ_{eff} for the subcutis being too low. When the absorption is too low, photons coming from a larger distance (sides of the bone) are not attenuated enough. Increasing μ_{eff} to an unreasonably high value (higher than tested in figure 10) shows Gaussian vessels, but the overall image becomes too dark.

C. Why is the MP area in some images much darker than in other images?

From the results in both figure 10 and 11 it can be seen that the used μ_{eff} for both subcutis and bone strongly influences the intensity of the tissue around the MP. All presented values are inside the SD range as found in literature, see appendix A. The origin of

varying μ_{eff} values are mainly tissue consistency (e.g. in subcutis: amount of fat cells, water, and connective tissue). Additionally, due to the geometrical differences between real fingers, the tissue depth d is varying as well. This gives that both the finger dimensions and the tissue consistency influence the intensity in the resulting image. This is a natural conclusion, since μ_{eff} and d are the two variables in the Beer-Lambert equation.

D. How can transmission of NIR light through the finger be modelled?

The procedure that is followed to mimic the light transmission is discussed in section V. Since the generated images roughly appear similar to the real images, it can be concluded that the realised approach is effective. The procedure can further be verified using the illuminated areas from figure 12. The resulting illuminated areas in the generated images are approximately the same as in the real images. The generated DIP area is slightly smaller. Assuming the anatomy is roughly the same in the model and real finger, the conclusion can be drawn that the model accurately mimics light transmission. The differences between the resulting areas may be the result of varying anatomy and different μ_{eff} values (see the previous research question in section VIII-C).

E. Can the original vessel templates be extracted from the generated images?

From the results in figure 13, it can be observed that the general shape of the especially the genuine distributions are similar. The high generated impostor scores cause the large EER. This may be explained by small elements in the original vascular template that are lost at the output of the model. This is visualised in appendix C by the binary templates of the original image and generated template at 0.25 mm depth (figures 14c and 14f). The latter appears a filtered version of the former. Excluding these elements results in higher impostor scores compared to when they are included. Thus, to answer the research question, the original template can be extracted to a certain extent. Small groups of pixels in the original template are not reproduced in the templates extracted from generated images.

F. Future work

The knowledge obtained by this thesis can be further applied in research on vascular biometrics. Identification based on finger vascular biometrics is currently solely based on the extracted vessel pattern (that sometimes includes the joint borders [20]). Nevertheless, including information such as the intensity of the bone and the vagueness of the vessels provides additional personal information. Incorporating this in the identification procedure may increase the performance.

Additionally, as briefly stated in the introduction, obtaining knowledge on the imaging procedure will contribute to the research on spoofing. Knowing how the image is exactly formed will help detecting synthetic images, or images from a fake finger.

This work can also be used to create a dataset containing synthetic images. Current finger vascular datasets are often limited by being small, their capturing procedure is insufficiently documented or they are not publicly available due to privacy concerns. A next step for this research would be to create custom vessel patterns. Ideally, more anatomical features are incorporated in the model as well, to make the created images appear more real. This synthetic dataset can be used to train machine learning architectures. The variables in the dataset can be manually adjusted, for example the addition of finger rotation. A classifier can be used to evaluate the effect that this variation has on the identification performance, since the parameters of the synthetic images are precisely known. Additionally, a synthetic set can be used to train a classifier to detect fake images, which is useful in research on spoofing.

IX. CONCLUSION

This research focuses on obtaining a better understanding of the imaging procedure for finger vascular biometric images. Many aspects in these images were unknown, including the width and vagueness of the vessel projection, the bright area of the joints and the dark area between the joints. In order to understand the imaging process, a simplified mathematical model is introduced to mimic the behaviour of near-infrared (NIR) light in the finger, including the bone, subcutis skin tissue and the vessel tree, to create finger vascular images based on real images.

The presented model is accurately able to mimic the vessel projection based on simplifying assumptions on the anatomy and optical parameters of the tissues. Features such as the bright joints and dark vessel projections are reproduced. It appears that the intensity of the areas of the joints and the area between the joints is directly related to the effective attenuation coefficient of both bone and subcutis. This coefficient depends on the tissue consistency of the subject. The appearance of the vessel projection is related to the vessel depth in the finger. In the situation where the vessel projection contains a full-shadow, the Gaussian shape of the vessel becomes

clearly visible. In this situation, there is relation between the width of the vessel projection and its depth in the model.

The model at this stage is a basic representation of a finger, limited by the simplifying assumptions made on the anatomy and optical variables. In order to improve the model further, the anatomy can be improved by including the shape of a real finger and by including additional tissues in the model.

X. Acknowledgements

References

[1] Andreas Uhl, Christoph Busch, Sébastien Marcel, and Raymond Veldhuis. *Handbook of vascular biometrics*. Springer Nature, 2020.

[2] B Ton. Vascular patern of the finger: biometric of the future? sensor design, data collection and performance verification. Master's thesis, University of Twente, 2012.

[3] Elmar Laistler, Matija Milanic, et al. Assessing spectral imaging of the human finger for detection of arthritis. *Biomedical optics express*, 10(12):6555–6568, 2019.

[4] Xi Li, Laura Petrini, Ruth Defrin, Pascal Madeleine, and Lars Arendt-Nielsen. High resolution topographical mapping of warm and cold sensitivities. *Clinical neurophysiology*, 119(11):2641–2646, 2008.

[5] Nadia Farinelli and Enzo Berardesca. The skin integument: variation relative to sex, age, race, and body region. *Handbook of non-invasive methods and the skin*, 2:27–31, 2006.

[6] Cynthia C Norkin and D Joyce White. *Measurement of joint motion: a guide to goniometry*. FA Davis, 2016.

[7] Fieke Hillerström, Ajay Kumar, and Raymond Veldhuis. Generating and analyzing synthetic finger vein images. In *2014 International Conference of the Biometrics Special Interest Group (BIOSIG)*, pages 1–9. IEEE, 2014.

[8] Hanwen Yang, Peiyu Fang, and Zhiang Hao. A gan-based method for generating finger vein dataset. In *2020 3rd International Conference on Algorithms, Computing and Artificial Intelligence*, pages 1–6, 2020.

[9] Antonia Creswell, Tom White, Vincent Dumoulin, Kai Arulkumaran, Biswa Sengupta, and Anil A Bharath. Generative adversarial networks: An overview. *IEEE Signal Processing Magazine*, 35(1):53–65, 2018.

[10] Kunfeng Wang, Chao Gou, Yanjie Duan, Yilun Lin, Xinhu Zheng, and Fei-Yue Wang. Generative adversarial networks: introduction and outlook. *IEEE/CAA Journal of Automatica Sinica*, 4(4):588–598, 2017.

[11] Amina Mokhtar. Generating 2d synthetic finger vein images. 2020.

[12] Dalibor Maljurič and Klemen Grm. Sensitivity analysis of finger-vein recognition models. *Elektrotehniski Vestnik*, 87(5):287–294, 2020.

[13] Naoto Miura, Akio Nagasaka, and Takafumi Miyatake. Feature extraction of finger-vein patterns based on repeated line tracking and its application to personal identification. *Machine vision and applications*, 15(4):194–203, 2004.

[14] Bram Ton. Miura et al. vein extraction methods. https://nl.mathworks.com/matlabcentral/fileexchange/35716-miura-et-al-vein-extraction-methods, 2022. Accessed on 2022-05-11.

[15] Nadya Ugryumova, Stephen John Matcher, and Don P Attenburrow. Measurement of bone mineral density via light scattering. *Physics in Medicine & Biology*, 49(3):469, 2004.

[16] Yangyang Liu, Yuyan Wang, Zhiyu Qian, Jinzhe Zhao, Xinzhi Cao, and Weitao Li. Monitoring the reduced scattering coefficient of bone tissues on the trajectory of pedicle screw placement using near-infrared spectroscopy. *Journal of Biomedical Optics*, 19(11):117002, 2014.

[17] Elena Vladimirovna Salomatina, Brian Jiang, John Novak, and Anna N Yaroslavsky. Optical properties of normal and cancerous human skin in the visible and near-infrared spectral range. *Journal of biomedical optics*, 11(6):064026, 2006.

[18] Steven L Jacques. Optical properties of biological tissues: a review. *Physics in Medicine & Biology*, 58(11):R37, 2013.

[19] Dirk J Faber, Maurice CG Aalders, Egbert G Mik, Brett A Hooper, Martin JC van Gemert, and Ton G van Leeuwen. Oxygen saturation-dependent absorption and scattering of blood. *Physical review letters*, 93(2):028102, 2004.

[20] Muriel van der Spek and Luuk Spreeuwers. Identification through finger bone structure biometrics. *and Signal Processing in the Benelux, May 20-21, TU Eindhoven*, page 56, 2021.

[21] C Rebecca Simpson, Matthias Kohl, Matthias Essenpreis, and Mark Cope. Near-infrared optical properties of ex vivo human skin and subcutaneous tissues measured using the monte carlo inversion technique. *Physics in Medicine & Biology*, 43(9):2465, 1998.

[22] Alexey N Bashkatov, EA Genina, VI Kochubey, and VV Tuchin. Optical properties of human skin, subcutaneous and mucous tissues in the wavelength range from 400 to 2000 nm. *Journal of Physics D: Applied Physics*, 38(15):2543, 2005.

[23] Victor George Peters, DR Wyman, MS Patterson, and GL Frank. Optical properties of normal and diseased human breast tissues in the visible and near infrared. *Physics in Medicine & Biology*, 35(9):1317, 1990.

[24] Alexey N Bashkatov, Elina A Genina, Vyacheslav I Kochubey, and Valery V Tuchin. Optical properties of human cranial bone in the spectral range from 800 to 2000 nm. In *Saratov Fall Meeting 2005: Optical Technologies in Biophysics and Medicine VII*, volume 6163, pages 306–316. SPIE, 2006.

[25] M Firbank, M Hiraoka, M Essenpreis, and DT Delpy. Measurement of the optical properties of the skull in the wavelength range 650-950 nm. *Physics in Medicine & Biology*, 38(4):503, 1993.

[26] Antonio Pifferi, Alessandro Torricelli, Paola Taroni, Andrea Li Bassi, Ekaterine Chikoidze, Eleonora Giambattistelli, and Rinaldo Cubeddu. Optical biopsy of bone tissue: a step toward the diagnosis of bone pathologies. *Journal of biomedical optics*, 9(3):474–480, 2004.

[27] Frédéric Bevilacqua, Dominique Piguet, Pierre Marquet, Jeffrey D Gross, Bruce J Tromberg, and Christian Depeursinge. In vivo local determination of tissue optical properties: applications to human brain. *Applied optics*, 38(22):4939–4950, 1999.

[28] Scott Alan Prahl. *Light transport in tissue*. PhD thesis, The University of Texas at Austin, 1988.

[29] Mahmood Kamali Moaveni. *A multiple scattering field theory applied to whole blood*. University of Washington, 1970.

[30] Setsuo Takatani and Marshall D Graham. Theoretical analysis

of diffuse reflectance from a two-layer tissue model. *IEEE Transactions on Biomedical Engineering*, (12):656–664, 1979.

[31] Annika MK Enejder, Johannes Swartling, Prakasa Aruna, and Stefan Andersson-Engels. Influence of cell shape and aggregate formation on the optical properties of flowing whole blood. *Applied optics*, 42(7):1384–1394, 2003.

[32] Igor V Meglinski and Stephen J Matcher. Quantitative assessment of skin layers absorption and skin reflectance spectra simulation in the visible and near-infrared spectral regions. *Physiological measurement*, 23(4):741, 2002.

[33] Cheng-Lun Tsai, Yi-Sheong Chou, and Jen-Yuan Tsai. Simulation of skin near-infrared reflectance spectrum. In *Laser-Tissue Interaction X: Photochemical, Photothermal, and Photomechanical*, volume 3601, pages 327–334. International Society for Optics and Photonics, 1999.

[34] Po-Hao Chen, Ke-Ching Chang, Shih-Hsin Ma, Jiann-Hwa Lue, and Ting-Jou Ding. Improvement of led non-invasive blood glucose meter. In *2018 1st International Cognitive Cities Conference (IC3)*, pages 250–252. IEEE, 2018.

[35] Aamir Shahzad, NM Saad, N Walter, Aamir Saeed Malik, and Fabrice Meriaudeau. An efficient method for subcutaneous veins localization using near infrared imaging. In *2014 5th International Conference on Intelligent and Advanced Systems (ICIAS)*, pages 1–4. IEEE, 2014.

[36] J Beuthan, U Netz, O Minet, Annerose D Klose, AH Hielscher, A Scheel, J Henniger, and G Müller. Light scattering study of rheumatoid arthritis. *Quantum Electronics*, 32(11):945, 2002.

[37] Adina E Draghici, Diane Potart, Joseph L Hollmann, Vivian Pera, Qianqian Fang, Charles A DiMarzio, J Andrew Taylor, Mark J Niedre, and Sandra J Shefelbine. Near infrared spectroscopy for measuring changes in bone hemoglobin content after exercise in individuals with spinal cord injury. *Journal of Orthopaedic Research®*, 36(1):183–191, 2018.

[38] Elina A Genina, Alexey N Bashkatov, and Valery V Tuchin. Optical clearing of cranial bone. *Advances in Optical Technologies*, 2008.

[39] Mathieu Dehaes, Kamran Kazemi, Mélanie Pélégrini-Issac, Reinhard Grebe, Habib Benali, and Fabrice Wallois. Quantitative effect of the neonatal fontanel on synthetic near infrared spectroscopy measurements. *Human brain mapping*, 34(4):878–889, 2013.

[40] Aya Abdelsalam. Modelling light interaction in healthy and degenerated articular cartilage. Master's thesis, Itä-Suomen yliopisto, 2021.

[41] Naoto Miura, Akio Nagasaka, and Takafumi Miyatake. Extraction of finger-vein patterns using maximum curvature points in image profiles. *IEICE TRANSACTIONS on Information and Systems*, 90(8):1185–1194, 2007.

[42] Wonseok Song, Taejeong Kim, Hee Chan Kim, Joon Hwan Choi, Hyoun-Joong Kong, and Seung-Rae Lee. A finger-vein verification system using mean curvature. *Pattern Recognition Letters*, 32(11):1541–1547, 2011.

[43] Joon Hwan Choi, Wonseok Song, Taejeong Kim, Seung-Rae Lee, and Hee Chan Kim. Finger vein extraction using gradient normalization and principal curvature. In *Image Processing: Machine Vision Applications II*, volume 7251, pages 359–367. SPIE, 2009.

[44] Huafeng Qin, Lan Qin, Lian Xue, Xiping He, Chengbo Yu, and Xinyuan Liang. Finger-vein verification based on multi-features fusion. *Sensors*, 13(11):15048–15067, 2013.

[45] Beining Huang, Yanggang Dai, Rongfeng Li, Darun Tang, and Wenxin Li. Finger-vein authentication based on wide line detector and pattern normalization. In *2010 20th international conference on pattern recognition*, pages 1269–1272. IEEE, 2010.

[46] Ajay Kumar and Yingbo Zhou. Human identification using finger images. *IEEE Transactions on image processing*, 21(4):2228–2244, 2011.

[47] R Prem Kumar, Rachit Agrawal, Surbhi Sharma, Malay Kishore Dutta, Carlos M Travieso, Jesús B Alonso-Hernández, et al. Finger vein recognition using integrated responses of texture features. In *2015 4th International Work Conference on Bioinspired Intelligence (IWOBI)*, pages 209–214. IEEE, 2015.

[48] Bernhard Prommegger, Christof Kauba, Michael Linortner, and Andreas Uhl. Longitudinal finger rotation—deformation detection and correction. *IEEE Transactions on Biometrics, Behavior, and Identity Science*, 1(2):123–138, 2019.

[49] Christoph Kauba, Jakob Reissig, and Andreas Uhl. Preprocessing cascades and fusion in finger vein recognition. In *2014 international conference of the biometrics special interest group (BIOSIG)*, pages 1–6. IEEE, 2014.

[50] Huafeng Qin and Mounim A El-Yacoubi. Deep representation-based feature extraction and recovering for finger-vein verification. *IEEE Transactions on Information Forensics and Security*, 12(8):1816–1829, 2017.

[51] Xianjing Meng, Xiaoming Xi, Gongping Yang, and Yilong Yin. Finger vein recognition based on deformation information. *Science China Information Sciences*, 61(5):1–15, 2018.

APPENDIX A

OPTICAL COEFFICIENTS FOR BIOLOGICAL TISSUES

TABLE III: Values for μ_a and μ'_s of human subcutis skin tissue at 850 nm in mm^{-1}. The bold value is an outlier.

Paper	μ_a	μ'_s	Amount	Sample
Salomatina 2006 [17]	0.1 ± 0.03	2 ± 0.2	10	Face, scalp, neck, back
Simpson 1998 [21]	$\mathbf{0.0085 \pm 0.004}$	1.12 ± 0.4	4	Abdominal, breast
Bashkatov 2005 [22]	0.103 ± 0.03	1.05 ± 0.35	Unknown	Abdominal
Peters 1990 [23]	0.08 ± 0.03	0.66 ± 0.34	7	Breast
Average including outlier	0.073 ± 0.044	1.21 ± 0.57		
Average excluding outlier	0.094 ± 0.013			

TABLE IV: Values for μ_a and μ'_s of bone samples at 850 nm in mm^{-1}.

Paper	μ_a	μ'_s	Sample
Bashkatov 2006 [24]	0.011 ± 0.002	1.873 ± 0.137	Cranial bone
Firbank 1993 [25]	0.025 ± 0.002	1.7 ± 0.1	Skull
Ugryumova 2004 [15]	0.02	2.1	Pig skull
Pifferi 2004 [26]	0.008	1.21	Calcaneus (heel)
Bevilacqua 1999 [27]	0.05 ± 0.02	0.9 ± 0.1	Skull
Average	0.023 ± 0.017	1.56 ± 0.49	

TABLE V: Values for μ_a and μ'_s of blood (HbO$_2$ and Hb) at 850 nm in mm^{-1}. The haemoglobin concentration is expressed in gram Hb/L.

Paper	μ_a	μ'_s	Sample	Concentration
Prahl 1988 [28]	0.57, 0.35	-	HbO$_2$, Hb	150
Moaveni 1970 [29]	0.56, 0.42	-	HbO$_2$, Hb	150
Takatani 1979 [30]	0.55, 0.43	-	HbO$_2$, Hb	150
Faber 2004 [19]	0.5, 0.4	1.93, 1.46	HbO$_2$, Hb	93
Enejder 2003 [31]	0.5	1.7	Whole blood	Average $\approx$ 127
Average	0.48 ± 0.079	1.70 ± 0.24		

TABLE VI: Values for the anisotropy factor g of various biological tissues.

Tissue	Anisotropy factor range	Literature
Subcutis	0.75 - 0.95	[32], [17], [21], [33], [3], [34], [35]
Phalanges	0.8 - 0.9	[36], [3]
Skull (for reference)	0.9 - 0.93	[15], [37], [38], [39]
Articular cartilage	0.9 - 0.97	[40], [3]

APPENDIX B
VESSEL EXTRACTION

TABLE VII: Overview of commonly used vessel extraction methods.

Literature	Method	Abbreviation
Miura 2007 [41]	Maximum Curvature	MC
Miura 2004 [13]	Repeated Line Tracking	RLT
Song 2011 [42]	Mean Curvature	Mean Curv.
Choi 2009 [43]	Principal Curvature	PC
Qin 2013 [44]	Difference Curvature	DC
Huang 2010 [45]	Wide Line Detector	WLD
Kumar 2011 [46]	Gabor Filter	GF
Kumar 2015 [47]	Local Binary Pattern	LBP

TABLE VIII: Overview of the EER percentage as presented in literature comparing multiple methods. The bold numbers are the best performing methods from that research.

Literature	MC	Mean Curv.	PC	DC	WLD	GF	RLT	LBP
Ton 2012 [2]	0.49	-	**0.37**	-	0.89	-	0.99	-
Prommegger 2019 [48]	**0.37**	-	0.77	-	0.92	1.02	-	-
Kauba 2014 [49]	**0.42**	-	-	-	2.87	-	1.64	5.03
Maljurivc 2020 [12]	**7.26**	-	-	-	14.99	-	18.17	-
Qin 2017 [50]	8.30	**4.20**	-	7.90	7.62	5.08	12.85	-
Qin 2013 [44]	10.9	7.44	-	**3.32**	-	5.79	-	-
Meng 2018 [51]	**2.65**	10.64	-	-	-	-	8.25	6.90
Their own results	0.0009	0.25	0.36	3.32	0.87	0.65	0.145	0.081

APPENDIX C
VESSEL DEPTH VARIATION

(a) Original image (cut).

(b) Normalised (hist. eq.).

(c) Original vessel pattern.

(d) Initial depth at PIP ≈ 0.25 mm.

(e) Overlap.

(f) Resulting vessel pattern.

(g) Initial depth at PIP ≈ 0.5 mm.

(h) Overlap.

(i) Resulting vessel pattern.

(j) Initial depth at PIP ≈ 0.75 mm.

(k) Overlap

(l) Resulting vessel pattern.

(m) Initial depth at PIP ≈ 1 mm.

(n) Overlap.

(o) Resulting vessel pattern.

(p) Initial depth at PIP ≈ 1.25 mm.

(q) Overlap

(r) Resulting vessel pattern.

(s) Initial depth at PIP ≈ 1.5 mm.

(t) Overlap
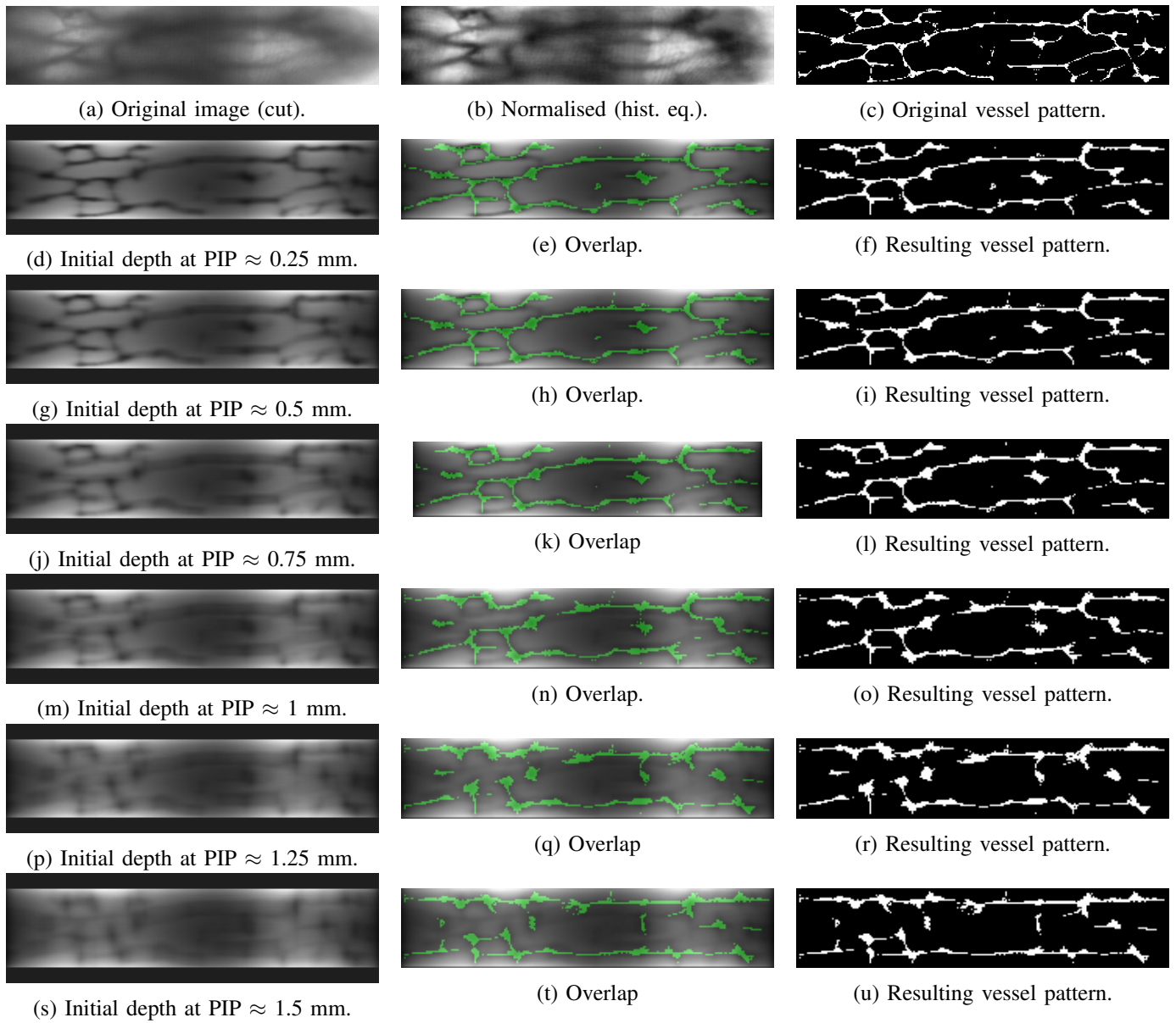
(u) Resulting vessel pattern.

Fig. 14: Visualisation of varying vessel depths and the resulting binary templates. The mentioned depth is the depth at the PIP joint, and increases 1.5 mm in the deepest point (shaft of the MP).

Fig. 15: Genuine and impostor similarity score distributions of the real dataset (a) and the generated image set (b). The respective plots of the FMR and FNMR over the classification error are given in (c) and (d). The corresponding DET-curves are given in (e) and (f).

(a) Same source image.   (b) Different source images.

Fig. 16: Similarity scores between real and generated images. For (a), each generated image is compared with the corresponding original image. For (b), each generated image is compared with the real images of that same finger, skipping the ones corresponding to the exact same image (which are covered for (a)). The mean for (a) is 0.520 ± 0.023, and for (b) 0.352 ± 0.065.